# DISPERSAL OF VOLCANIC ASH ON MARS:

# ASH PARTICLE SHAPE PARAMETER ANALYSIS

A THESIS SUBMITTED TO
THE GEOLOGY AND GEOPHYSICS DEPARTMENT

Submitted as part of a Bachelor of Science degree completed May 11th 2018

MAY 2018

By

Zachary T. Langdalen

Thesis Advisor

Sarah Fagents

We certify that we have read this thesis and that, in the opinion, it is satisfactory in scope and quality.

Thesis Advisor

Dr. Sarah A. Fagents
Hawai'i institute of Geophysics and Planetology

## Dedication

First, I want to thank my family for pushing and supporting me to apply myself through the complications of life. Without my advisor, Dr. Sarah Fagents, and her confidence and patience with me, I would not have been able to present and publish research as an undergraduate. Erin Fitch provided lots of feedback for this project, in addition to graduate school and career advice. It takes a community of support to complete such a huge task and I could not have done it without everyone.

# Acknowledgments

This project would not have been possible without the use of Dr. Gary Huss's optics laboratory. All data collection was performed using his equipment and lab space for sample preparation. Sample ash grains from the Hekla 1104 AD eruption were graciously provided by Dr. Maria H. Janebo, while the Rauðhólar ash grains were supplied by Erin Fitch. This project was funded in part by the NASA Space Grant Fellowship program.

# Abstract

The objective of this project was to create a representative database of the dimensions and shapes of volcanic ash particles in size divisions ranging from 1 mm to 64 μm, using a novel high-resolution automated microscopy procedure adapted from a protocol previously developed at the University of Hawaiʻi (Ogliore and Jilly, 2013). By compiling a database of ash particle dimensions and shapes, we will then be able to statistically estimate the effective cross-sectional areas and their variability as a function of particle size for use in a model of ash deposition on Mars. The optical system used for this study captures a series of images as the microscope stage moves upwards, and employs focus-stacking to capture elements that have a structure extending above the depth of field of a single image. Once the image mosaics are captured and processed, I use the program ImageJ to calculate particle dimensions. Using this method, I can provide the necessary range of dimensionless shape parameters required to calculate effective particle cross-sections affected by the atmospheric gas during fallout, and apply these results to an ash settling model developed by Dr. Sarah Fagents. The final, improved model will ultimately be used to re-examine in a more sophisticated manner the possibility that Martian volcanoes were responsible for the formation of fine-grained, layered deposits that cover extensive areas of the surface of Mars. By aiming to quantify the impact of explosive volcanism on Mars, this project fulfills the NASA Solar System Workings Program goal of identifying "the physical variations in volcanic activity throughout the Solar System."

# Table of Contents

# List of Tables

# List of Figures

# 1. Introduction

The surface of Mars hosts large areas of fine-grained, friable, layered deposits (Greeley et al., 2000). The origins of these deposits have been debated in the literature; they have been proposed to relate to volcanic, fluvial, or eolian systems (Greeley et al., 2000). We propose to determine the credibility of a volcanic ash source producing layered formations. Simulation of volcanic eruptions to determine where ash particles emitted from a known source would be deposited will allow for a more thorough evaluation of the explosive volcanism hypothesis. Comparing the locations and extents of the known layered deposits to the estimated areas of ash deposition will determine which features could plausibly be explained as ash fall deposits, and link those deposits to potential source volcanoes.

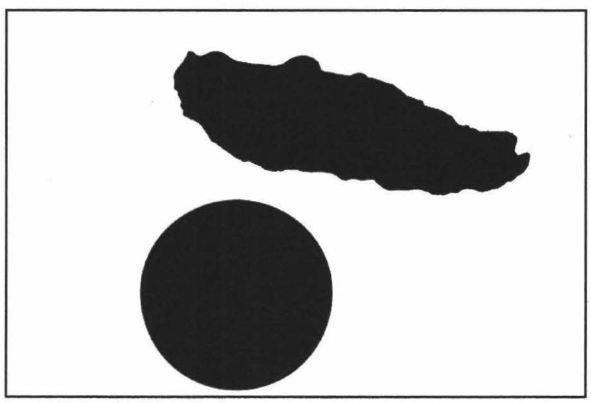

**Figure 1**. Binary image comparing a natural ash grain to a sphere with the same cross-sectional area. This visually demonstrates the disconnect between current ash dispersal models (which typically assume spherical particles) and the real situation.

Current volcanic ash dispersal models make many assumptions to simplify the mathematical complexity of the problem and provide a tractable and efficient solution to the equations governing particle dispersal and deposition. For example, major simplifications are applied to the shape and heterogeneity of the erupted tephra. Many models make the assumption that ash grains are perfect spheres; however, as shown in **Figure 1**, natural ash morphologies can be highly irregular. We argue that the assumption of spherical grains in ash dispersal and deposition models will have a significant impact in the prediction of how far ash will be deposited from the eruption source. As can be seen from **Figure 2**, the drag coefficients, $C_d$, of non-spherical particles tend to be significantly greater than those of spheres. In addition, rough surfaces experience greater

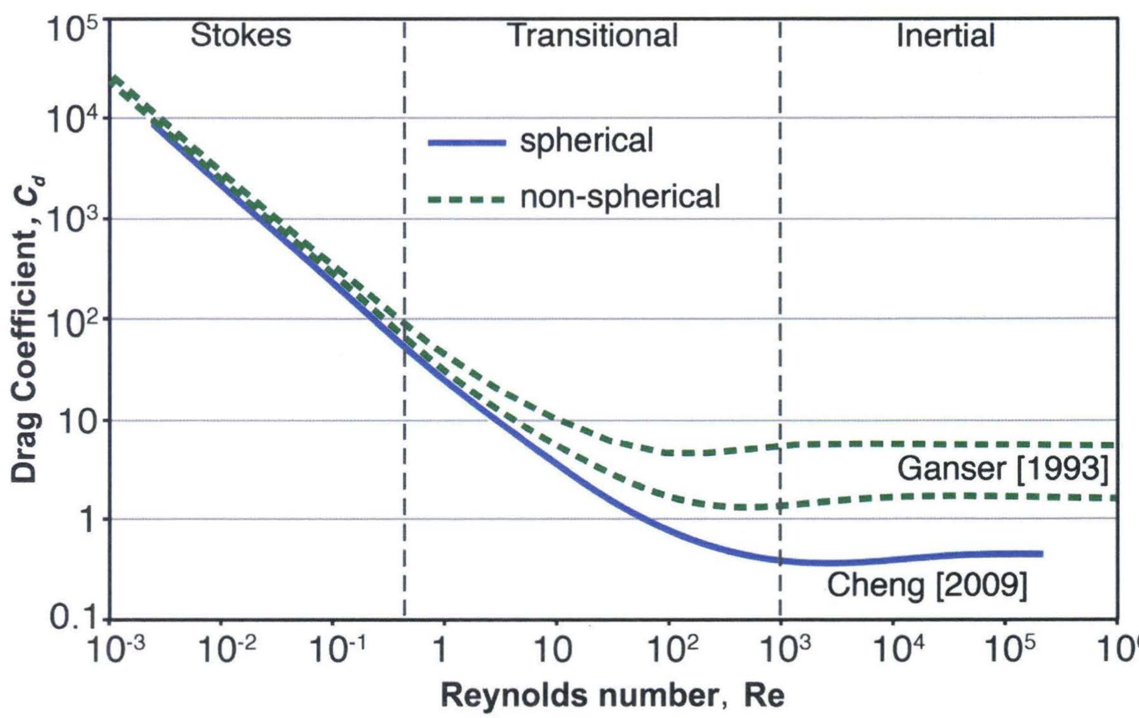


**Figure 2**. Plot of drag coefficient as a function of particle Reynolds number (Re = $\rho_a ud/\mu_a$, where $\rho_a$ and $\mu_a$ are the density and viscosity of the atmosphere, and $d$ and $u$ are the diameter and fall velocity of the particle) for spherical (blue solid line) and non-spherical particles (green dashed line).

drag in a flowing fluid medium than smooth surfaces. Together, the factors lead to lower settling velocities, longer fallout times, and the potential to be dispersed in the wind field over greater distances. Therefore, the extents of deposits predicted based on the assumption of smooth, spherical clasts may be substantially underestimated.

To make progress toward the goal of better representing drag forces acting on volcanic particles, I have imaged ash grains from terrestrial eruptions to create a database of shape parameters of natural ash morphologies. Shape parameters are unitless ratios that quantitatively measure geometric features. This database of shape parameters will be used to develop improved treatments of particle drag in ash settling models (Fagents et al., 2017), thereby allowing more accurate computation of the dispersal extents of Martian explosive eruptions.

This thesis presents my approach in development of a methodology to quantify the morphologies of natural ash particles. In the Background section, I first summarize the geology and volcanism of Mars as motivation for developing this study. I then lay out the methods I developed to capture, process, and analyze images of ash particles ranging in diameter from 1 mm down to 62 μm. The Results section focuses on two shape parameters, aspect ratio and convexity, that best represent the overall shape and surface irregularity of ash grains. The Discussion section covers my interpretations for this study. The Conclusions section is followed by a Future Work section, in which I summarize a variety of ways in which this study could be extended.

# 2. Background

Although Mars appears to lack volcanic activity in the present day, its surface is replete with volcanic features, including enormous shield volcanoes and vast lava plains, indicating volcanism was widespread in the past (Greeley et al., 2000). Today the surface of Mars is a cold and dry desert (Greeley et al., 2000); the current atmosphere is 5.6 mbar, which means that any water exposed on the surface of the planet would rapidly vaporize (Greeley et al., 2000). It has not always been this way, as evidenced by the vast fluvial networks and outflow channels which attest to the presence of voluminous surface waters at some point in Mars history.

The Martian geologic timescale consists of three main divisions: the Noachian (prior to ~3.8 Ga), Hesperian (3.8 Ga to 3.0 Ga) and Amazonian (3.0 Ga to present) (Greeley et al., 2000). The Noachian period shows global volcanism transitioning to focused vent eruptions in the Tharsis, Elysium and Circum-Hellas plains. Around 1.6 Ga ago the eruptions became focused in the Tharsis region with widespread lava flows and explosive eruptions (Werner, 2009). Extensive volcanism continued on Mars until 100–200 Ma years ago (Greeley et al., 2000). Examination of Mars' global volcanic history shows a transition from ancient, explosive edifices constructed in the southern highlands to later shield- and plains-forming volcanism in the northern lowlands. This may reflect a loss of interior volatiles over time; nevertheless, studies of northern features suggest that explosive volcanism was a component of later-stage volcanism (Greeley et al., 2000).

With a mean radius of 3390 km, Mars is a significantly smaller planet than Earth (6371 km), giving it distinct geophysical characteristics such as lower gravity, and leading to an absence of plate tectonics due to more rapid cooling (Greeley et al., 2000). Combined with the lower atmospheric pressure, these parameters produced eruptions that behaved significantly different from terrestrial volcanism, leading to systematic differences in the characteristics of the resulting volcanic features. For example, the lack of plate motion allows volcanoes to become very large on Mars: Olympus Mons, the largest shield volcano in the solar system, is 6000 km in diameter whereas terrestrial shields rarely exceed 700 km. Furthermore, on Mars, the combination of lower gravity and a lower atmospheric pressure increase the eruptive energy produced from the expansion of a given volume of magmatic gases (Greeley et al., 2000). This implies greater explosive energies than produced by terrestrial volcanic systems, resulting in widespread dispersal of ash.

### 2.1 Origin of fine-grained deposits on Mars

The morphologies of volcanic features on Mars' surface have long been interpreted as representing generally mafic (i.e. basaltic) magmas. Compositional information returned by a fleet of Mars spacecraft since the 1990s generally confirm this interpretation, although Bandfield et al. (2000) identified a "Surface Type 2", which they suggested was consistent with a basaltic andesite to andesitic composition. Alternatively, this surface type might represent a weathering product of basalt. Nevertheless, even if Mars volcanism was entirely mafic, there are reasons to believe that explosive volcanism on Mars would have been much more vigorous than on Earth. The lower confining pressure of the atmosphere means exsolving magmatic volatiles would have experienced much

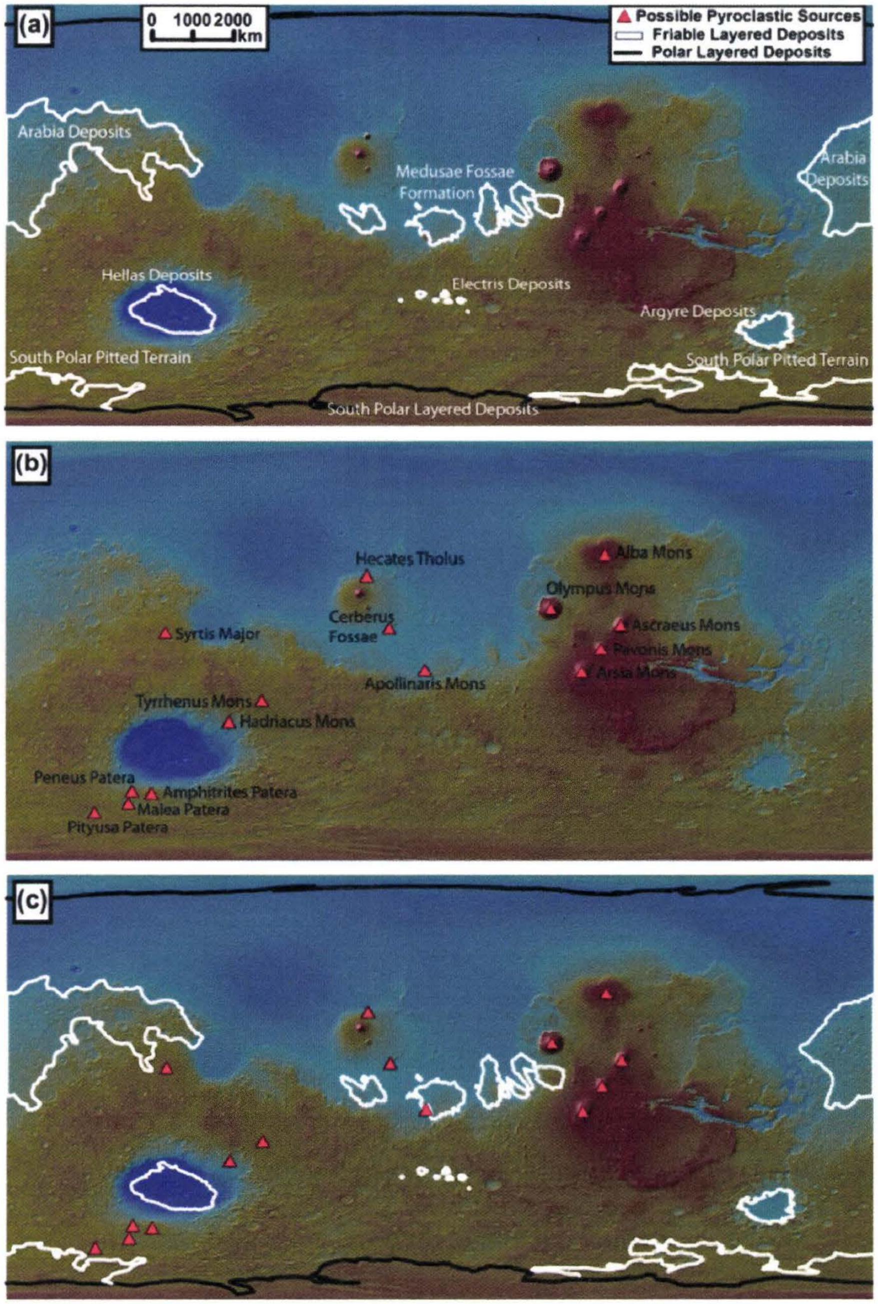


**Figure 3**. Map of the fine-grained deposits from Kerber et al. (2013) comparing locations of volcanic vents likely to be associated with explosive volcanism and fine-grained deposits. Map A shows the deposits, Map B shows the volcanic vents used in the Kerber et al. (2013) study, and Map C shows both overlaid on the same map.

greater decompression, allowing for much greater exsolved gas volumes, thorough magma fragmentation, and greater acceleration of eruptive products as the gas phase expanded down to the low ambient pressure. Even if Martian magmas were volatile poor compared to terrestrial basaltic examples, explosive volcanism should have been common. On exiting the vent, the competing effects of (i) lower atmospheric pressure reducing drag forces on ash grains (leading to higher settling velocities compared to Earth), and (ii) lower gravity reducing settling velocities compared to Earth, will dictate the subsequent dispersal area of the deposit.

Deposits relevant to this study include the Medusae Fossae Formation (MFF), Valles Marineris, chaotic terrain, Terra Meridiani and Arabia materials (**Figure 3)**. The Medusae Fossae Formation, for example, has been observed and categorized as radically different in texture since the earliest images of Mars became available (Bradley et al., 2002). With an estimated volume of 1.4 x $10^6$ $km^3$, the MFF is bedded and contains irregularly consolidated sediments draped over the overlying topography. The Formation appears relatively smooth and features layering at a regional scale (Bradley et al., 2002). Consistent lineations interpreted as wind eroded yardangs (**Figure 4**), with orientations varying depending on the stratigraphic height (Scott and Tanaka, 1982), attest to the friable nature of these deposits.

The origins of these friable, layered deposits have long been debated. Possibilities include fluvial, volcanic, or eolian sources (Edgett, 1997; Malin and Edgett, 2000; Bradley et al., 2002). There are issues with each hypothesized origin. Fluvial reworking is observed inside of formations such as the MFF, demonstrating its presence in the past. However, the scale of the fluvially reworked features is small compared to the entire MFF, which suggests the fluvial system present was not capable of generating such a large amount of sediment. Volcanic vents and extensive explosive volcanism could have provided air-fall tephra that could comprise the fine-grained deposits. The fixed location of the vents and distribution of the fine-grained deposits raises the question of whether it is even possible for the known vents to deposit the material where it is found today. Eolian processes still occur on the cold, dry Martian surface today, as shown by the yardangs in **Figure 4**. This evidence of reworking from surface winds demonstrates the presence of wind necessary for saltation but does not provide evidence for strong enough winds to create or transport the sediment needed for the entire formations.

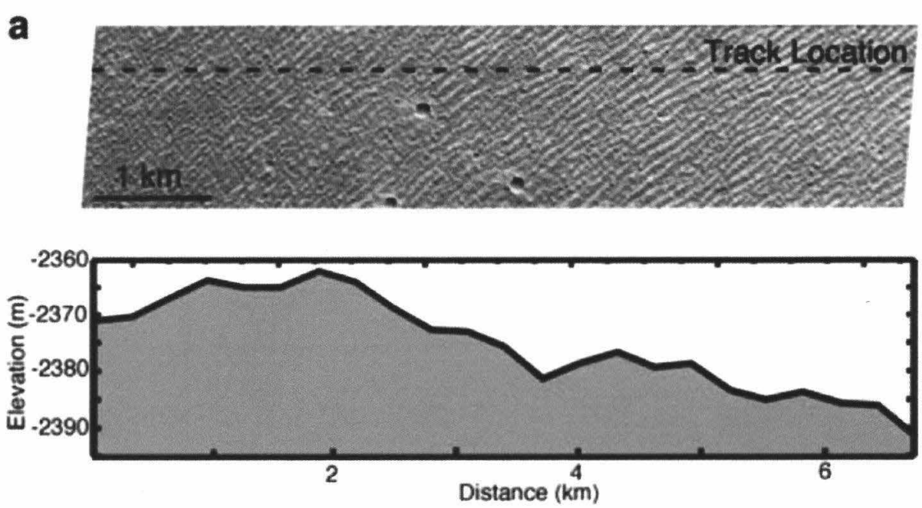


**Figure 4**. MOC image M0201173 of MFF “ridge and valley” terrain showing abundant yardangs. The MOLA track line displayed with the dashed line in the image provides the elevations shown in the bottom elevation graph (Kerber et al., 2013).

The Medusae Fossae Formation overlies volcanic vents and cones possibly as young as 10 Ma (Hartmann and Neukum, 2001), which further supports the formation originating from a fall deposit of volcanic origin (Bradley et al., 2002). Furthermore, the location of volcanic vents close to the MFF and presence of material <2 mm in size further support the hypotheses that formations such as the Medusae Fossae Formation are of volcaniclastic origin.

### 2.2 Previous ash dispersal modeling

Linking vents to specific deposits and time periods, using a rigorous treatment of the details of volcanic particle settling, will provide valuable information on the volcanic history of Mars. The lack of physical samples and the global extent of friable, layered deposits provide a key opportunity for modeling of tephra dispersal to better understand the nature of the planetary deposits.

Kerber et al. (2013) used a simplified settling model coupled to a Mars General Circulation model to examine the fate of ash released into the atmosphere from numerous potential source volcanoes. Kerber et al. (2013) addressed the formation of the MFF Hellas, Arabia, and Electris deposits (Figure 3). For the MFF, they determined that Olympus, Ascraeus, Pavonis and Arsia Montes, Elysium Mons, Cerberus Fossae, and Apollinaris Mons could all have contributed volcanic material. The estimated amount of material, $1.4 \times 10^6$ $km^3$, making up the MFF is comparable to the cumulative erupted volume totals from the possible vents. Although the estimated extent of the deposits predicted by the (Kerber et al., 2013) model was not an ideal fit with the location of the MFF, the fit was sufficient to allow them to propose that volcanic formation of the MFF is consistent with Apollinaris Mons, Arsia Mons, and Pavonis Mons being the most likely candidates. As shown in **Figure 5,** the fit between the predicted and observed deposits is not perfect, leaving some of the MFF with insufficient predicted deposit thickness, and demonstrating the need to take a more complex modeling approach to better evaluate the validity of the volcanic hypothesis.

Among the deficiencies of the Kerber et al. (2013) approach are (i) the treatment of particles as spheres, (ii) adoption of a typical particle size (10 or 30 μm) that is likely too small to represent the average particle size of the deposit, (iii) particle release heights that are probably too large (see Glaze and Baloga (2002) for a discussion of the limits on convective plume rise on Mars), and (iv) the assumption that ash particles are perfectly coupled to the wind field during dispersal when in fact they almost certainly lag behind. These factors suggest that the dispersal distances predicted by Kerber et al. (2013) are misrepresented to an extent that merits reexamination of the problem.

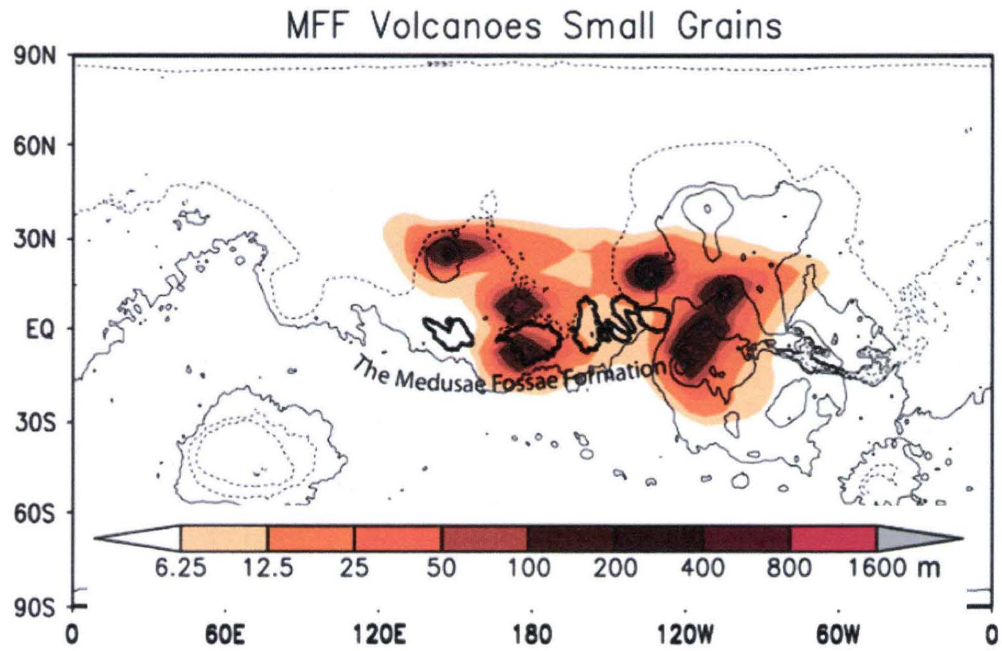


**Figure 5**. Output of Kerber et al. (2013) simulation showing dispersal of ash volume of $1.4 \times 10^6$ km$^3$ in the Medusae Fossae Formation.

Building a more realistic model requires the addition of theory to account for processes such as tumbling, grain accretion, non-continuum effects in the rarified Martian atmosphere, and drag coefficients of natural ash grain shapes. These processes have competing effects, with some producing higher particle settling velocities and others leading to lower settling velocities. To determine the overall influence on settling velocities, each must be examined in turn. Here, I start with natural ash grain morphologies that are not represented by models such as Hynek et al. (2003) and Kerber et al. (2013), which underpredict particle drag forces and lead to higher settling velocities. To better treat the true morphologies of natural ash grains in drag relationships, the challenge is to turn qualitative shape features into quantitative values. Deriving improved ash grain drag relationships, from a set of shape parameters derived from a natural grain set large enough to be statistically relevant, will provide a more representative treatment of the ash plume and dispersal and deposition of the ash grains.

# 3. Methods

This study included two main phases of data acquisition as I developed, tested, and refined the methodologies required to acquire a robust data set of shape parameters suitable for ash samples.

## 3.1 Determination of Relevant Shape Parameters

Descriptive terms for ash grains used by volcanologists, such as mossy, fluidal, vesicular and blocky, exist on a spectrum, making them inadequate for the detail needed for modeling ash dispersal and deposition. To solve both the terminology issue and need for quantitative data, I acquired shape parameters from images of natural ash grains. Shape parameters are unitless relationships between two geometric quantities, such as axis lengths, particle perimeter, or projected area. In this study, I tested the use of parameters such as *roundness*, *compactness*, *rectangularity*, *perimeter*, *cross-sectional area*, and *sphericity* for the most appropriate descriptors of natural ash particles (**Table 1)**. For example, roundness describes how comparable the two-dimensional projected particle shape is to a mathematically perfect circle. I found roundness to not be an ideal candidate for describing surface irregularity because even the volcanic grains closest to being a perfect circle feature surface roughness that affects the flow of gases over the surface. Fluidal grains, with their smooth surfaces and elongate shapes, could rank lower than a rough-textured circular grain in terms of roundness. This highlighted the need to test multiple shape for natural ash grains of multiple morphologies.

**Table 1.** Comparison of shape parameters calculated for this project.

| Shape Parameter | Formulae | Attribute represented |
|---|---|---|
| Circularity | Four pi times the area of the equivalent circle divided by the perimeter squared | Irregularity/ roughness |
| Aspect Ratio | Major axis length divided by the minor axis length | Elongation |
| Roundness | The perimeter squared divided by 4 pi times the grain area | Irregularity/ roughness |
| Solidity | Grain area divided by the convex hull area | Irregularity/ roughness |
| Convex Hull Area | Area of the convex hull based on the major and minor axes that encloses the grain | Irregularity/ roughness |
| Convex Perimeter | Perimeter of convex hull that encloses the grain based on the major and minor axes | Irregularity/ roughness |
| Convexity | The convex hull perimeter divided by the actual grain perimeter | Irregularity/ roughness |

For example, to describe the degree of elongation seen in the natural ash grain in comparison to the sphere (**Figure 1**), I chose aspect ratio, which compares the lengths of the major and minor axes. A value greater than one indicates shapes that are elongated with respect to a sphere, which features perfect symmetry.

During the first phase of this study I acquired seven different shape parameters to create a test grain data set in order to determine which shape parameters represented features that were desirable to describe. Starting with the major difference between the natural ash grain in **Figure 1** and the sphere used to approximate settling particles, I targeted two main parameters to describe elongation and surface roughness. Elongation, or the degree of which the magnitude of major axis is enlarged relative to the minor axis, is well represented by *aspect ratio*: (major axis length)/(semi major axis length). Surface irregularity, or the small-scale protrusions that create the complex jagged surface seen on natural volcanic ash grains, is well represented by *convexity* (perimeter of grain / perimeter of the best fit ellipse).

### 3.2 Sample Selection

#### *Phase 1*

The objective of phase 1 of the study was to define a rigorous and repeatable methodology for capturing ash grain morphology. In phase 1, I selected the sample set from ash recovered from a rootless tephra cone within the Rauðhólar cone field. Rauðhólar is located in a 5200-year-old Elliðaá lava flow southeast of the capital of Iceland, Reykjavík. These rootless cones were formed when lava flowed into a lake producing explosive lava–water interactions (Fitch et al., 2017). Rauðhólar tephra was chosen because it provided us with readily available ash grains in desirable sizes, with a wide range in particle morphologies that would provide a robust test of the methodology. I chose five grains spanning the range of observed morphologies **(Figure 6).** The ash features red lacustrine clay coating the outside of the grains. **Figure 6** also demonstrates a key problem with limited microscope depth of field and complex ash morphologies creating regions out of focus.

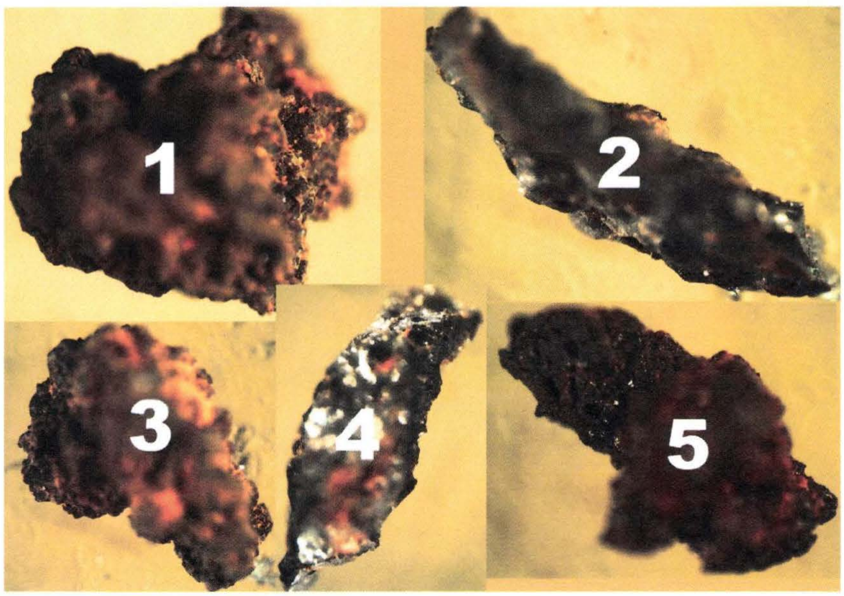


**Figure 6**. Reflected light image of the five 1ϕ grains selected from the Rauðhólar rootless cone group for use in the initial methodology investigation.

***Phase 2***

In phase 2, I selected grains from ash recovered from the eruption of Hekla in 1104 AD. Although this eruption was of rhyodacite composition (Janebo et al., 2016), it was chosen as a relatively high-intensity analog for Martian basaltic eruptions because of the inferred likelihood that such eruptions would have been systematically more explosive under conditions of low atmospheric pressure (Greeley et al., 2000). The higher silica content of the magma created a more viscous melt, increasing resistance to flow of the melt, which together with the higher volatile content, led to a more energetic fragmentation process. Similarly, Martian basaltic eruptions into a low atmospheric pressure environment would have led to greater explosion energy compared to a terrestrial basaltic eruption (Greeley et al., 2000). For this investigation, I chose this higher energy eruption because high energy eruption products are likely to be a comparable analog to ash produced in Martian explosive eruptions.

Phase 2 built on experience gained from analyzing the morphologies of the Rauðhólar ash. Comparing shape parameter values with individual grain morphologies, I employed the methodology for image capture and processing developed in phase 1 on a larger sample set. Generating a statistically relevant sample set captured in greater detail through adapting Ogliore and Jilly's (2013) novel image mosaic technique was the major goal. For the Hekla 1104 AD eruption set I analyzed five size fractions from 0ϕ to 4ϕ (i.e., $d = 1$ mm to 62 μm; where $\phi = -\log 2d$, with $d$ in mm). The Wentworth phi scale is a logarithmic scale of classification for volcanic ejecta (White and Houghton, 2006). Material is determined to fall within a size bin if it fits through a mesh, meaning it is less than "X" by "X" dimensions on two axes. This means that elongate 0ϕ grains are less than 1 mm on two axes but can have a length of greater than 1 mm along the major axis. For each size bin, I randomly selected 30 grains from a sieved sample set of ~100 grains. To limit selection bias from subjective instincts to pick the most interesting shapes that would lead to a non-representative sample, I used an obscuring technique. Grains were chosen through an unfocused microscope providing only enough clarity to manually manipulate the grains.

## 3.3 Sample Preparation

For phase 1, the test grain set was selected from a sample pre-sieved set of 0ϕ Rauðhólar ash grains, chosen to represent the entire range of morphologies displayed in the sample set. The selected samples (**Figure 6**) were manipulated with forceps and mounted using double-sided tape adhered to a glass slide. Grains were repositioned between exposures with the adhesive providing enough support for semi-permanent mounting.

For phase 2, I changed the selection process and increased the sample size. For each size bin (0ϕ to 4ϕ) of the Hekla sample, the 30 grains were again mounted on glass slides using double-sided tape. Grain map images of the completed slides were used for reference and identification of the individual grains (**Figure 7**). Each grain map is annotated with the compositional classification (pumice, dark/lithic grains, or free crystals) to which each grain was assigned.

## 3.4 Image Acquisition

### *Phase 1*

To create a database of shape parameters that can be used in mathematical ash dispersal modeling, I imaged ash grains mounted on a clear slide with double-sided tape as the adhesive. The use of tape for adhesive allowed the grain to be repositioned on the slide for the capture of grain morphology in three orthogonal (A, B, C) orientations. The grains conditions of low atmospheric pressure (Greeley et al., 2000). The higher silica content of the magma created a more viscous melt, increasing resistance to flow of the melt, which together with the higher volatile content, led to a more energetic fragmentation process. Similarly, Martian basaltic eruptions into a low atmospheric pressure environment would have led to greater explosion energy compared to a terrestrial basaltic eruption (Greeley et al., 2000). For this investigation, I chose this higher energy eruption because high energy eruption products are likely to be a comparable analog to ash produced in Martian explosive eruptions.

Phase 2 built on experience gained from analyzing the morphologies of the Rauðhólar ash. Comparing shape parameter values with individual grain morphologies, I employed the methodology for image capture and processing developed in phase 1 on a larger sample set. Generating a statistically relevant sample set captured in greater detail through adapting Ogliore and Jilly's (2013) novel image mosaic technique was the major goal. For the Hekla 1104 AD eruption set I analyzed five size fractions from 0ϕ to 4ϕ (i.e., $d$ = 1 mm to 62 μm; where $\phi = -\log 2d$, with $d$ in mm). The Wentworth phi scale is a logarithmic scale of classification for volcanic ejecta (White and Houghton, 2006). Material is determined to fall within a size bin if it fits through a mesh, meaning it is less than "X" by "X" dimensions on two axes. This means that elongate 0ϕ grains are less than 1 mm on two axes but can have a length of greater than 1 mm along the major axis. For each size bin, I randomly selected 30 grains from a sieved sample set of ~100 grains. To limit selection bias from subjective instincts to pick the most interesting shapes that would lead to a non-representative sample, I used an obscuring technique. Grains were chosen through an unfocused microscope providing only enough clarity to manually manipulate the grains.

## 3.3 Sample Preparation

For phase 1, the test grain set was selected from a sample pre-sieved set of 0ϕ Rauðhólar ash grains, chosen to represent the entire range of morphologies displayed in the sample set. The selected samples (**Figure 6**) were manipulated with forceps and mounted using double-sided tape adhered to a glass slide. Grains were repositioned between exposures with the adhesive providing enough support for semi-permanent mounting.

For phase 2, I changed the selection process and increased the sample size. For each size bin (0ϕ to 4ϕ) of the Hekla sample, the 30 grains were again mounted on glass slides using double-sided tape. Grain map images of the completed slides were used for reference and identification of the individual grains (**Figure 7**). Each grain map is annotated with the compositional classification (pumice, dark/lithic grains, or free crystals) to which each grain was assigned.

## 3.4 Image Acquisition

### *Phase 1*

To create a database of shape parameters that can be used in mathematical ash dispersal modeling, I imaged ash grains mounted on a clear slide with double-sided tape as the adhesive. The use of tape for adhesive allowed the grain to be repositioned on the slide for the capture of grain morphology in three orthogonal (A, B, C) orientations. The grains

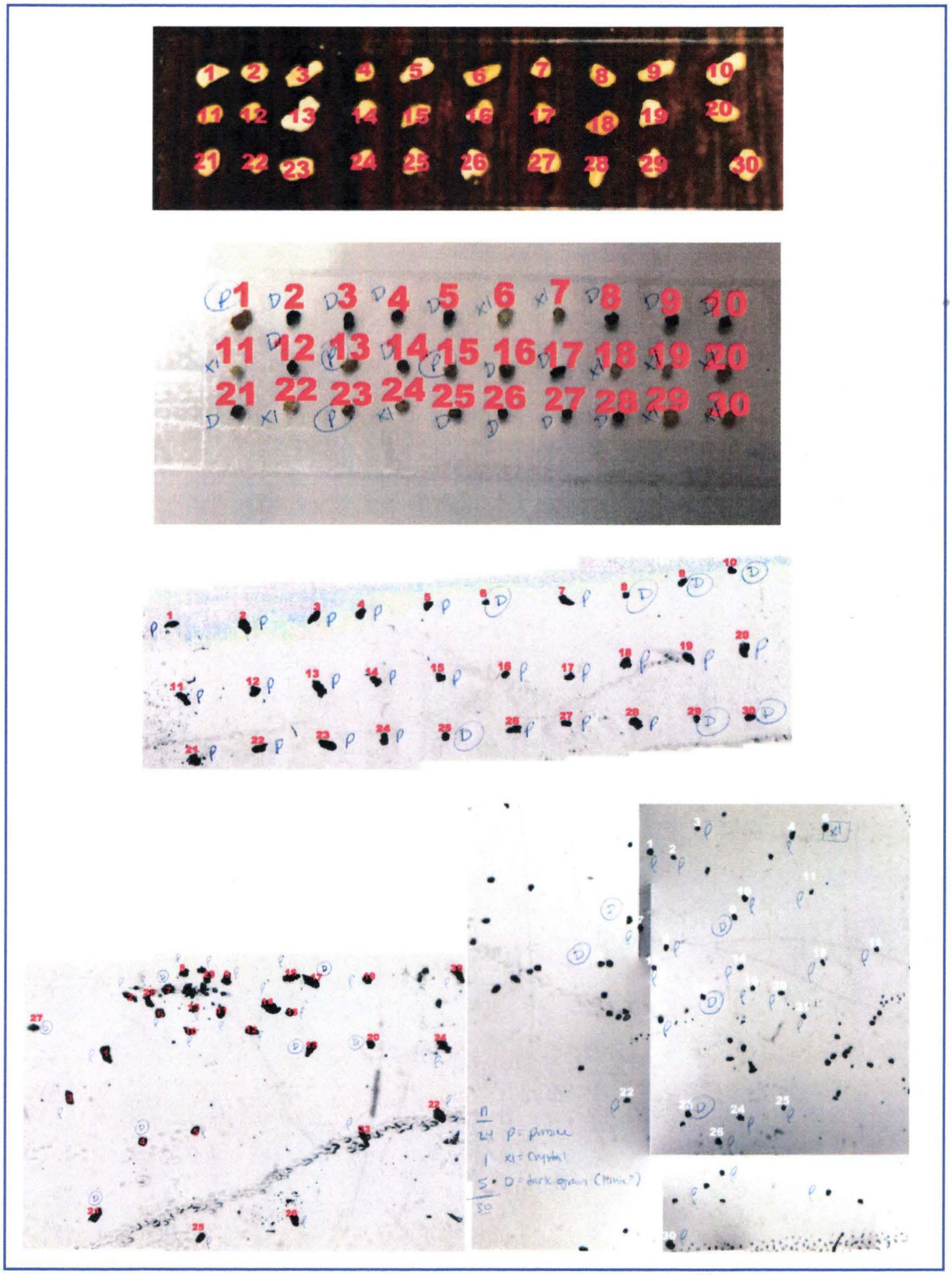

**Figure 7**. Grain maps of the 0ϕ (top), 1ϕ, 2ϕ, 3ϕ, 4ϕ (bottom) slides. Composition of each grain is labeled with P for pumice, XL for crystals, and D for dark/lithic grains.

were manipulated using forceps to find the "major face" which displayed the largest grain area and was termed the A orientation. The B orientation of each grain was found by holding the grain by the major axis and rotating 90 degrees. The C orientation or minor face is the smallest grain area that is found rotating the grain along the minor axis 90 degrees. **Figure 8** displays how this approach captures all unique elements in three dimensions for a simple rectangle. Images were captured with backlight illumination creating a dark silhouette representing the grain. In phase 1, I used the Nikon KMZ 1500 microscope with an Optronics Microfire camera to take single exposures of the outline of each grain under transmitted light. The Optronics Microfire camera with the zoom setup chosen to capture the range of 0ϕ grains produced a resolution 375 pixels/mm in the final jpeg images.

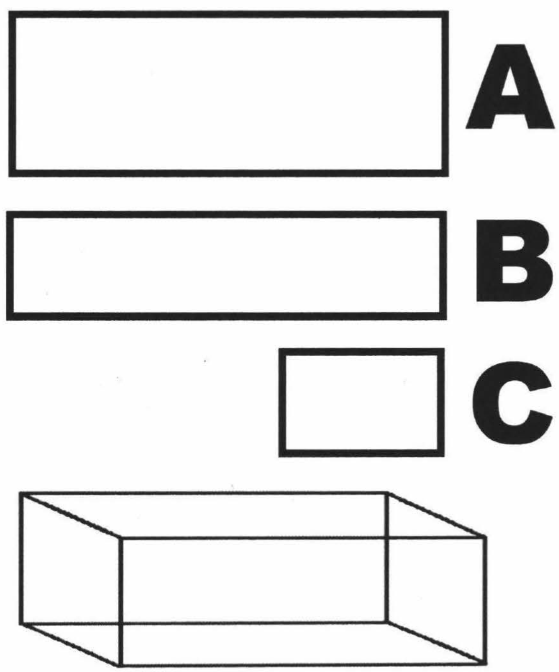


**Figure 8**. Diagram showing three views of a cuboid captured with the A, B, C positioning technique.

### *Phase 2*

For phase 2, image acquisition technologies developed by Ogliore and Jilly (2013) were used as guidance. Microscope lenses have a limited depth of field, which makes capturing irregular grain edges entirely in focus impossible to accomplish on a whole grain set. To work around this physical limitation, I employed digital processing to combine images taken at different focal heights to effectively broaden the depth of field to encompass the entire grain outline in focus. By encompassing the entire grain outline I was able to make better binary representations of each grain with less noise added during processing.

I employed a Nikon AZ 100 microscope with an automated stage, transmitted light source and Cannon T2i camera attached to capture silhouette images. This set-up was balanced on an air stabilization table and all integrated on a computer tower running Linux. The range of z-axis heights that encompassed all elements of each grain was determined manually prior to image acquisition, by finding highest and lowest in-focus edge elements. The range was then divided by five to find the z-axis step size between each image. The choice of five z-axis steps per grain was made to keep the data storage and processing at a manageable level, while still capturing a clear in-focus outline. Images were captured starting at the top of the in-focus range with an even step size in between each image. The camera recorded jpeg images sized 5184 pixels × 3456 pixels, i.e., ~18 megapixels. Physical resolution varied from 3,000 pixels per mm to 12,000 pixels per mm over the different grains as different zoom levels were employed to capture different sized grains.

I developed an "image stacking" technique to combine all of the in-focus portions of multiple images of an individual grain. The technique utilized Adobe Photoshop CS6 Running on a MacBook to merge the microscope jpeg images. Each grain was imaged at multiple z-axis heights with the same x and y position. The images, termed a "Stack", are then imported into Photoshop and layered on top of each other. The *auto align* and *auto blend* tools are used to produce a final mosaic made up of only the in-focus sections of each grain. The mosaic image is saved as a flat one-layer jpeg image,

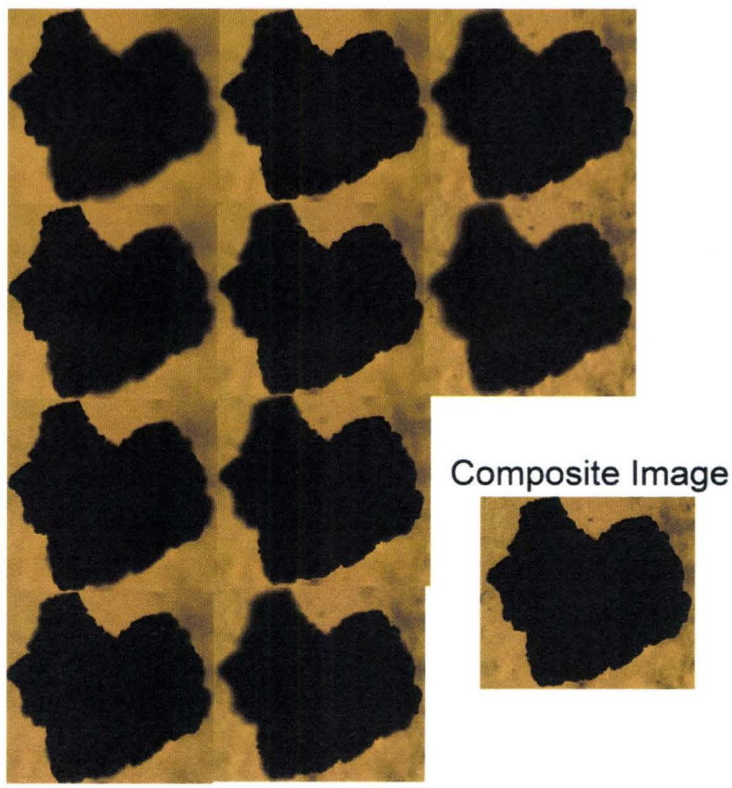


**Figure 9**. Composite showing 10 images taken at multiple z-axis heights combined into one image through overlaying in Adobe Photoshop. The individual images lack focus on some portions of the outline, whereas the composite image shows the outline nearly completely in focus.

then converted to binary and run through ImageJ to measure shape parameters. Comparison of **Figure 6** to **Figure 9** shows that the edge focus detail is substantially increased through the employment of image stacking.

The depth of field of produced by the microscope depends on the amount of zoom being used – depth of field decreases as a greater zoom is employed. Throughout analyzing grains that range from 0ϕ to 4ϕ, I found it necessary to use a total magnification range of 2x to 24x.

### 3.5 Image Processing

#### *Phase 1*

Raw color images of the backlit view of each grain in the A, B and C orientations were captured on the Optronics Microfire camera connected to a PC running Windows XP. Images were captured in jpeg format and imported onto a MacBook Pro running Adobe Photoshop CS6 for processing. Once imported, each image's color profile was changed to grayscale. The images were then converted to binary by applying the threshold tool at a value between the light and dark peaks in data number (DN) distributions specific to each image (**Figure 10**). Manual clean-up of anomalous features such as isolated dark spots and interior gaps was sometimes required. The final grain outline binary files were saved in jpeg format prior to being imported to ImageJ for shape parameter measurement. ImageJ is a geometric measurement software package (https://imagej.nih.gov/ij/index.html) used in scientific image processing that calculates shape parameters such as area, perimeter, circularity, aspect ratio, roundness, solidity, convex hull area, convex hull perimeter, and convexity (**Table 1**). I used a micrometer slide to determine the ratio of physical space to digital pixels, and ImageJ uses this scale to output physical measurements such as area (in $mm^2$) and perimeter (in mm), in addition to the shape parameters.


**Figure 10**. Use of thresholding tool to create binary images. This image displays a strong contrast between light and dark pixels, as shown by the bimodal distribution of data numbers in the inset histogram. Some noise remains in the upper right-hand section of the image; this is removed manually to enable automated acquisition of shape parameters using ImageJ

***Phase 2***

For each grain there are multiple images corresponding to the number of different vertical stage positions needed to capture all portions of the grain in focus. Once the images were downloaded from the camera SD card they were renamed with the following format: Grain_Side_Image number. For example, G6_A_3.jpg is the 3rd image from the highest in-focus element of grain 6 on the major face. Once renamed, the files are batch imported into Photoshop using File >> Scripts >> Load Images into a stack, then selecting the number of images that make up the vertical image stack for an individual grain. Once loaded into a stack, each image layer is selected prior to selecting Edit >> Auto Align Layers. In the options for Auto Align Layers, *Auto* is selected with none of the additional options. The result of the this process aligns all layers of the stack ready to blend. White space may be visible or a change in the size of the image dimensions may occur. While the layers are still all selected, Edit >> Auto Blend Layers is used to select *Stack Images* with the *Seamless Blending* option. After rendering, the composite image produced is made up of the in-focus elements of each image is complete. The composite image file is saved under the naming scheme Grain_Side.psd, for example G6_A.psd. An additional copy is saved in jpeg format which discards the layer information, creating a file ready to be converted to binary.

Opening the previously completed composite image jpeg file in Adobe Photoshop, the process for conversion to a binary image starts with Image >> Mode >> Grayscale to discard the color information. Once in grayscale, the background layer is selected and a *Duplicate Layer* is created using the default name. The background duplicate layer is selected before selecting Image>>Adjustment>>Threshold. The resulting histogram displays two distinct brightness peaks, representing the dark grain and bright background of the sample slide. Once thresholded, removal of any remaining dark artifacts using the pencil tool leaves the slide ready to be saved as Grain_Side_Bin. jpg.

Micrometer images that were acquired to generate an image scale for each individual zoom level are then opened in Photoshop. The ruler tool is used to measure the distance in pixels between smallest tick marks. The tick mark gaps correspond to 0.01 mm so placing the pixels /0.01 mm gives the ratio of pixels to mm. The physical resolution pixel to mm ratio is needed for ImageJ to provide measurements of physical quantities such as area or perimeter in mm.

The jpeg binary images are imported into ImageJ and processed one final time to ensure they are binary. The scale determined from the micrometer images is input and the shape descriptors to be measured are set prior to analyzing the particles. ImageJ is then run to compute the shape parameters. The dimensions are saved in Microsoft Excel format, and the information for each individual grain is then combined onto a master spreadsheet.

# 4. Results

***Phase 1***

After acquiring the shape parameters from the initial five grain Rauðhólar test set, which were selected to display the greatest extent of unique morphologies, I plotted the values produced and compared the morphological features to shape parameter values. In phase 1, elongation and surface irregularity were targeted as morphological features that I sought to find corresponding shape parameters for. Shape parameters were calculated for the individual A, B, and C orientations for each grain, and an average was calculated to describe the grain as a whole. The five grains were ranked based on the averages of each shape parameter, in order to distinguish the presence of a given shape characteristic (**Figure 11**).

*Aspect ratio* describes the degree of elongation of the major axis in comparison to the minor axis, with a value of one indicating a completely equant grain. Morphologies of the five Rauðhólar ash grains ranged from fairly equant to bladed with substantial elongation, providing a wide base of sample morphologies on which to evaluate shape parameters. I obtained individual grain orientation values (A, B, or C) ranging from 1.122 to 3.485, with average values between 1.21 and 2.36 (**Figure 11**). The morphologic differences among each orientation and each grain produced significantly different aspect ratio values, indicating the usefulness of taking images of three sides.

*Convexity* describes the degree of surface irregularity by comparing the perimeter of the grain to the perimeter of the grain's convex hull, with a value of one indicating a grain with no surface irregularity. The Rauðhólar ash grains all displayed surface irregularities (Figure 11), with 0.92 being the highest value (least irregular) produced. Overall, I obtained individual grain orientation values (A, B, or C) ranging from 0.81 to

0.92, with average values between 0.83 and 0.9. The spreads of convexity values from among each grain's orientations were fairly consistent. Notably, grain 2 produced a spread of ~0.1, with the A-orientation value being drastically different from the B- and C-orientations. Convexity did not exhibit a clear trend when changing from equant to elongate orientations.

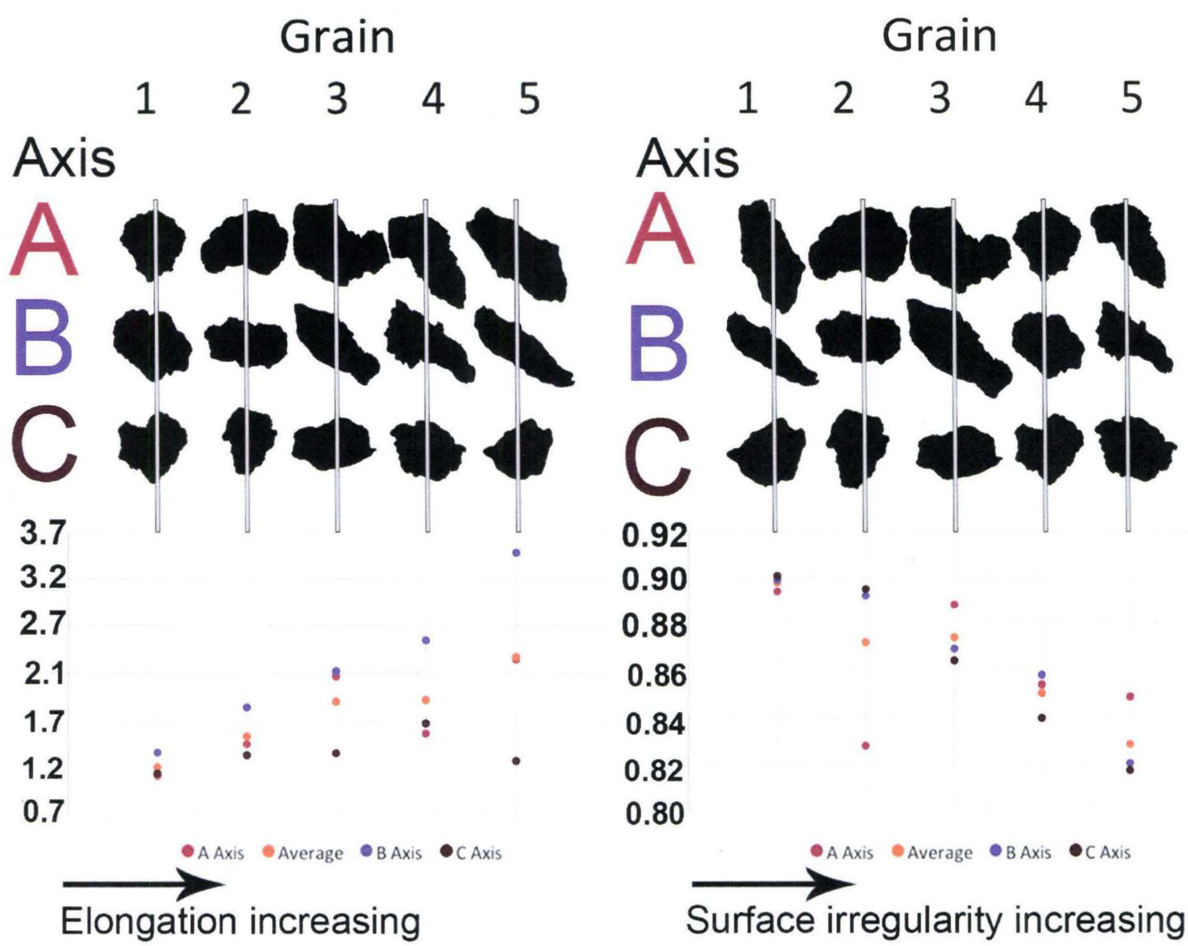


**Figure 11**. The results from phase 1 showing the binary silhouette of each grain in all three orientations, with the corresponding aspect ratio value on the left, and the convexity values on the right.

*Phase 2*

For phase 2, I investigated grains from 0ϕ to 4ϕ, imaging 30 grains per size bin. Some grains did not provide a clean outline in the image (due, for example, to dust or particle fragments adhering to the mounting tape) and were removed from the study to prevent the introduction of errors in the analysis. This left at least 22 grains per size bin that were included in the analysis, for a total of 131 grains. This larger sample size allowed generation of a statistically robust data set, in comparison to the small five-grain test set of phase 1. Appendix A gives the data captured for the full 131 grain set.

To further examine the variation of shape in the samples, different lithologic components comprising the samples were identified and quantified. **Figure 13** shows that the Hekla 1104 AD sample features dominantly pumice and dark/lithic grains, with crystals being a subordinate member. Pumice grains are highly vesicular clasts produced by the volatile-rich rhyodacite magma. Lithic/dark grains are pieces of angular, dense wall rock that was eroded and entrained into the erupting gas–particle mixture. Crystals are grains made entirely of phenocrysts that grew in the magma reservoir prior to eruption, and which were liberated from the melt phase during fragmentation.

Proportions of each ash type vary with bin size (**Figure 12**). At the 2ϕ, 3ϕ, and 4ϕ size bins (average grain projected areas of 0.177, 0.039, and 0.007 $mm^2$, respectively), pumice is dominant, making up ~ 80% of the total grains. Dark/lithic grains are secondary, making up almost all of the remaining 20%, with the crystals composing a fraction less than 1%. The componentry reverses at the 1ϕ size bin (0.45 $mm^2$), where pumice is the lowest at ~15%, crystals are present at ~25% and dark/lithic grains dominate at ~50% of the total grains. In the 0ϕ size bin (0.552 $mm^2$), pumices make up

100% of the grains sampled. Because the grains were chosen at random from each size bin, the overall percentage of each lithology should closely mirror the total proportions present in the larger sample.

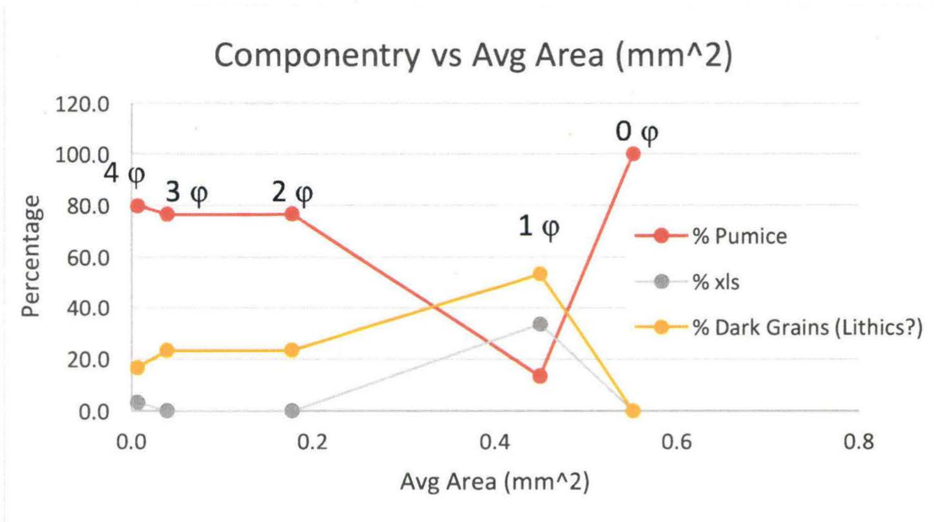


**Figure 12**. Proportion of each ash component (pumice, crystals (xls) and dark/lithic grains) plotted against average projected grain area for each ϕ size class. The individual points plotted represent approximately the median size of grains in each size bin. There is a notable decrease in the proportion of pumice clasts at a grain size of 0.45 $mm^2$.

Aspect ratio and convexity were again plotted for the 131 grain Hekla sample set. To identify any pattern of elongation with grain size, aspect ratio was plotted against grain size in **Figure 13**, with each lithology indicated by different symbol colors. Because the exact sizes of grains in each ϕ size bin vary, I chose to plot the shape parameters against the projected cross-sectional area of the grains to provide a more detailed comparison for those grains for which the areas overlaps two ϕ size bins. On each plot the linear slope fitting tool in Microsoft Excel was used to plot a linear trendline; the line of best fit equation and Coefficient of Determination $R^2$ are given on the plots. $R^2$ is a statistical quantity that displays how close the data points are to the best fit line. $R^2$ values cannot be greater than one, with a value of one indicating every point plotted is exactly along the line of best fit. $R^2$ values greater than 0.7 are considered strong correlations, values 0.5 – 0.7 display a moderate correlation, and values 0.5 – 0.3 are considered weakly correlated, with values less than 0.3 displaying negligible correlation.

All 131 grains in the phase 2 investigation are accounted for in the fitting of the trendline, which has a very shallow slope (-0.127) and an $R^2$ value of 0.0041, indicating

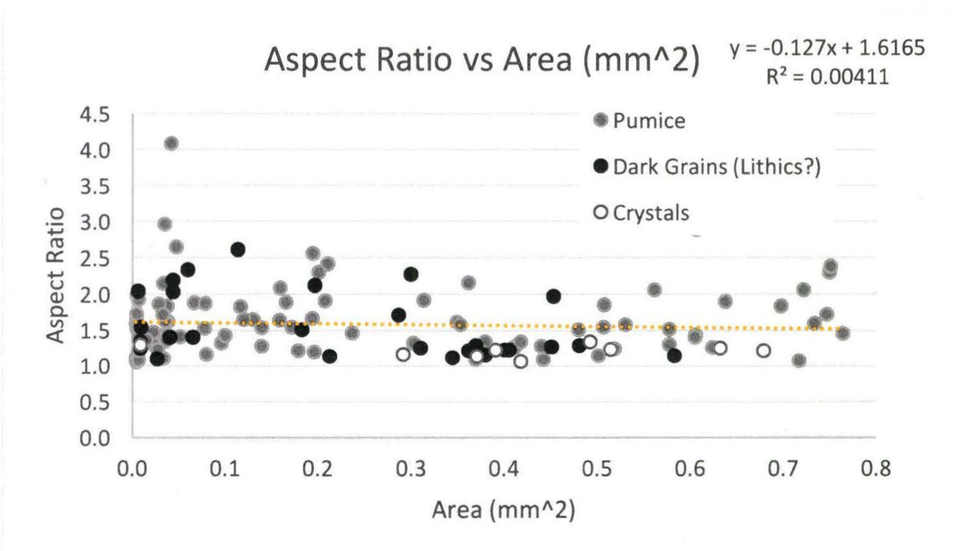


**Figure 13**. Plot of aspect ratio vs. projected grain area for all 131 grains included in phase 2. Symbol colors depict different ash components: black symbols represent dark, lithic grains; gray symbols represent pumice and white symbols are free crystals. A linear trendline (orange, dashed) shows that there is no correlation between aspect ratio and grain area.

negligible correlation, and therefore a negligible tendency for elongation to vary with grain size. However, some patterns are found in the individual lithologic subsets. The crystal ash particles show a consistent pattern of aspect ratio values of less than 1.5 across all size fractions. Aspect ratio values close to 1 quantify the tendency of crystals to be equant across all size fractions.

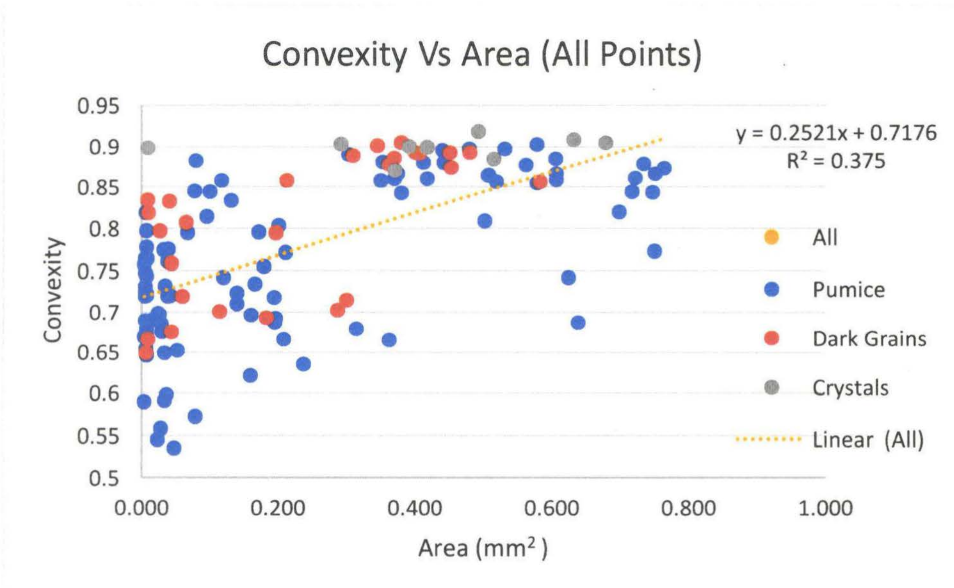


**Figure 14**. Plot of convexity versus area of all grains in the 131-sample phase 2 investigation. Data points are color coded by grain lithology; the trend line is calculated for all grains.

Convexity is the shape parameter most sensitive to surface irregularity. It is defined as the ratio of the perimeter of the convex hull enclosing the grain, and the perimeter of the grain itself. Values close to 1 indicate a smooth surface texture, whereas values less than 1 indicate the presence of surface irregularity. **Figure 14** plots convexity against grain area for all ash grains measured in phase 2, with a best fit linear regression accounting for all grain measurements. The trend line shows a positive slope with a $R^2$ value of 0.375 indicating weak correlation of convexity with grain size. Larger convexity values indicate a smoother, less irregular surface and the positive trend observed shows larger grains exhibiting less surface irregularity. Conversely, smaller grain sizes exhibit greater surface irregularity. None of the ash grains measured in this study produced convexity values of 1, demonstrating the irregularity present in natural ash grains at all scales.

## 5. Discussion

The results from both phases 1 and 2 indicate clearly that natural ash grains exhibit elongation and surface roughness that make spheres poor analogs for ash dispersal modeling. Elongate, irregular shapes can spin and tumble chaotically in freefall, and surface roughness affects the flow of atmospheric gases over the grain surfaces, both influencing the resulting drag forces. To obtain accurate drag coefficients, the possibility of tumbling and the effect of the turbulence created from surface roughness must be accounted for. To do this, an effective cross-sectional area can be calculated based on the data collected for this project. The extended period of time that ash stays in a low-density atmosphere like that of Mars means that, if the drag coefficients are underestimated by not taking into account tumbling or surface roughness, the predicted dispersal areas could be smaller than in reality.

The elongate nature of ash grains shown in the aspect ratio results (**Figures 11, 13**) is drastically different than the homogenous spheres used in previous ash dispersal simulations, such as Hynek et al. (2003) and Kerber et al. (2012, 2013). The data show that natural volcanic ash grains measured for phase 2 exhibit a significant and measureable degree of elongation compared with spheres used in the previous simulations. Elongate grains can tumble when falling, increasing drag forces that would keep ash grains in the atmosphere longer, traveling further distances.

Surface irregularities of volcanic ash grains would inhibit smooth laminar flow of atmospheric gases over the grain surfaces, which would act to increase drag forces, and potentially increase dispersal distances. Surface irregularity, as measured by grain convexity, were also present in all ash grains measured (**Figure 14**), with no grains producing a convexity value of 1 (the values for a smooth sphere). Larger grains demonstrated a greater degree of surface irregularity. The increase in resolution needed to image smaller grains with roughly the same number of pixels as larger grains may affect the amount of surface irregularity that is measured. Small surfaces irregularities that exist on $0\phi$ grains that are imaged at a resolution of ~4,000 pixels per mm may not be detectable, whereas the $4\phi$ grains that are imaged at ~12,000 pixels per mm become more sensitive to those asperities. However, the trend shows that smaller grains have fewer irregularities, so I am confident that the resolution issue is at the very least overpowered by the real changes, and that the technique adequately measures surface irregularities of larger grains.

# 6. Conclusions

The aim of this project was to gather detailed information on ash grain sets in various sizes from terrestrial eruptions. By developing strategies to capture the ash grain shapes in more detail and gather data on how the shape of the grain would experience atmospheric drag, I sought to provide the ash sedimentation modeling community a more complete picture on particle drag characteristics. The varied and irregular shapes of volcanic ash grains clearly demonstrate the need for a quantifiable measurement to better inform sedimentation models in order to draw conclusions on the origin of the friable deposits on Mars surface.

Determining a methodology for quantifying morphological features of volcanic ash grains and acquiring initial results has clearly demonstrated the need for ash sedimentation models to use more representative particle shape analogs than spheres. Developing and testing the three-axis (A, B, C) grain imaging protocol and image stacking techniques for their effectiveness on real ash grains has shown that microscope image shape analysis can provide the detailed quantitative morphological information needed to improve ash sedimentation models. Although the process can be time consuming, with the changes implemented during this project, I have increased efficiency to acquire sufficient data within a timeframe of 45 days to make statistically robust observations of trends.

The phase 1 study clearly quantified the differences between spheres and natural ash grains by recording seven unique shape parameters. Measuring the geometries of particle images in three unique orientations enabled more detailed analysis of the grains in three dimensions and of how surface roughness and elongation vary both for individual particles and among different particles. Combining the data from phases 1 and 2, changes in shape parameter values are clearly seen among both different grains and different grain orientations. From the small, five-grain sample set of the Rauðhólar ash, it appears that measuring the perimeter of a grain imaged in only one orientation misses a substantial component of the grain morphology. Performing the re-orientation manipulation, together with the image stacking protocol of phase 2, on a statistically relevant sample size would provide a more complete picture of how much ash grains vary with axis orientation, as well as from grain to grain.

In phase 2, I found no trend of elongation increasing or decreasing with grain size for the 131-grain Hekla 1104 AD rhyodacite sample. However, I did find that crystal grains tended to be quite equant across all size bins, with aspect ratios values less than 1.5. Surface irregularity of the ash grains, as measured by convexity, did show a trend of decreasing with decreasing grain size. The linear trendline that shows decreasing surface roughness has an $R^2$ value of 0.375 indicating moderate correlation.

The results of Kerber et al. (2012, 2013), using a model that treated ash particles as spheres, showed that it was not straightforward to match observed friable, layered deposits with source volcanoes. However, irregular, non-spherical particles experience greater drag, in part because of tumbling and spinning behaviors. The increased drag experienced by natural ash particles could help to account for the lack of an ideal fit between models and observations. The irregular and elongate nature of natural ash particles demonstrates the need to modify dispersal models with better treatments of particle drag, in order to further investigate the origins of deposits for which volcanism remains a viable mechanism (Bradley et al., 2002).

# 7. Future Work

This project was primarily one of developing methodologies for imaging and measuring ash grain morphologies. As such, the focus was on hardware, software, and techniques rather than on scientific interpretation of multiple ash samples. However, the preliminary interpretations presented in this thesis provide a basis on which to build by extending this analysis to other explosive deposits. Investigation of samples from additional deposits should be performed because composition and eruption intensity might influence the morphologies and surface texture of ash grains to a degree that merits accounting for treatments of aerodynamic drag in ash sedimentation models. I therefore hope to build on this project by imaging and analyzing additional ash grain sets. Specifically, I want to image basaltic ash deposits, closer in composition to what is found on Mars. Additional data points will help to explore the control of magma composition vs. eruptive energy and fragmentation mechanism on ash morphologies.

As this process has been refined, I have greatly reduced the time necessary to obtain shape data and look to be able to fully map, image, process, and compile one 30 grain sample in a single work day. Using this rate, I also hope to add additional size bins, such as ½ $\phi$ intervals, bringing the total number of grains per sample to 240 over 8 size bins.

The current protocol is a cost-effective means of quantifying ash grain morphologies. A microscope with no maintenance fees was used, together with a consumer grade camera that could be replaced for less than $1000 after its lifespan of ~120,000 image exposures. Processing is done through Adobe Photoshop CS 6, ImageJ, and Microsoft Excel, all programs that do not have large licenses fees. This keeps the costs down to essentially just the time of someone to perform the operations. In contrast, use of a scanning electron microscope (SEM) incurs a huge upfront cost, in addition to hourly costs, and does not necessarily convey advantages in terms of resolutions. Using the current approach, resolutions of 4,000–12,000 pixels per mm (depending on the zoom level) were obtained, which were more than sufficient to reveal small grain asperities.

To overcome the biggest limitation of processing with so many manual steps, development of a complete automated program would be a good investment. The automated program would take an input range where the mounted grain is physically located, find the focus point where most of the grain is clearly defined and take images above and below that point. Once the image stack is captured it would automatically combine the image and output one image ready to be measured in ImageJ. The actual processing time of each grain minus the cues required from the operator is ~2 minutes per image, meaning that a fully automated approach could rapidly process samples of hundreds of grains. The advantage of this would be reducing user input time allow imaging of more grains per size bin or integrate the A, B, C three-axis grain orientation imaging protocol used in phase 1.

The lack of physical Martian samples necessitates the analysis of multiple terrestrial deposits to take into account any changes in morphology created by compositional and eruptive energy differences. The substantial difference between Earth's and Mars' atmosphere alone may create systematic differences in eruptive products (e.g., size, morphology), so that we are unlikely to find a perfect terrestrial analog. Producing a larger database of eruptions of varying conditions will allow comparison of shape parameters to determine which factors have greater control over grain morphology.

Integrating the A, B, C three-axis image capture protocol into the phase 2 stacking technique was simply too time consuming to be done during this initial methodology study. By reducing the time required to stack and process each image into a binary outline of the grain morphology, imaging each grain's three axes would be feasible. A resolution increase was achieved of over an order of magnitude, from ~400 pixels per mm in phase 1 to 4000-12000 pixels per mm in phase 2. The additional resolution with the extended depth of field from the image stacking technique will give better definition of each grain's morphology from all three angles.

In short, reducing the time required to image each grain to the processing steps required would allow acquisition of data larger data sets and implementation of more complex ways to capture the grain in three dimensions. The ability to capture even more data points would allow investigation of rarer morphologies observed in phase 2 as outliers. Using 30 randomly sampled grains per size bin in this study, I expect to have observed all grain types that represent more than 3% of the total. Accelerating processing speed to capture 100 grains in three dimensions would permit analysis of grain types representing $\geq$ 1% of the total population, with improved clarity from focus stacking and three dimensional information about each grain.

# Appendix A

**Table A1.** All 131 data points from phase 2 showing the lithology, area, convexity, and aspect ratio. P = pumice (yellow cells in table), D = dark lithics (brown cells), xl = crystals (orange cells).

| | Grain | Area | Componentry | Convexity | Aspect Ratio |
|---|---|---|---|---|---|
| **0 phi** | 1 | 0.698 | P | 0.819 | 1.832 |
| | 2 | 0.578 | P | 0.855 | 1.303 |
| | 3 | 0.750 | P | 0.773 | 2.294 |
| | 4 | 0.412 | P | 0.88 | 1.264 |
| | 5 | 0.722 | P | 0.861 | 2.055 |
| | 6 | 0.751 | P | 0.866 | 2.377 |
| | 7 | 0.442 | P | 0.88 | 1.087 |
| | 8 | 0.380 | P | 0.842 | 1.339 |
| | 9 | 0.607 | P | 0.866 | 0.372 |
| | 10 | 0.374 | P | 0.867 | 0.819 |
| | 11 | 0.350 | P | 0.858 | 0.630 |
| | 12 | 0.531 | P | 0.897 | 0.648 |
| | 13 | | P | | |
| | 14 | 0.440 | P | 0.896 | 1.275 |
| | 15 | 0.562 | P | 0.877 | 2.054 |
| | 16 | 0.507 | P | 0.864 | 1.539 |
| | 17 | 0.370 | P | 0.86 | 1.088 |
| | 18 | 0.734 | P | 0.879 | 1.598 |
| | 19 | 0.606 | P | 0.859 | 1.429 |
| | 20 | 0.605 | P | 0.885 | 1.394 |
| | 21 | 0.578 | P | 0.903 | 1.516 |
| | 22 | 0.303 | P | 0.89 | 1.314 |
| | 23 | 0.747 | P | 0.843 | 1.721 |
| | 24 | 0.353 | P | 0.881 | 1.578 |
| | 25 | 0.480 | P | 0.897 | 1.506 |
| | 26 | 0.624 | P | 0.742 | 1.252 |
| | 27 | 0.764 | P | 0.873 | 1.448 |
| | 28 | 0.508 | P | 0.865 | 1.855 |
| | 29 | 0.519 | P | 0.856 | 1.239 |
| | 30 | 0.717 | P | 0.844 | 1.064 |
| **1 phi** | 1 | | P | | |

| | | | | | |
|---|---|---|---|---|---|
| | 2 | | D | | |
| | 3 | | D | | |
| | 4 | | D | | |
| | 5 | | D | | |
| | 6 | | xl | | |
| | 7 | | xl | | |
| | 8 | | D | | |
| | 9 | 0.451 | D | 0.893 | 1.261 |
| | 10 | 0.362 | D | 0.878 | 1.209 |
| | 11 | 0.391 | xl | 0.9 | 1.223 |
| | 12 | 0.401 | D | 0.893 | 1.221 |
| | 13 | 0.638 | P | 0.687 | 1.898 |
| | 14 | 0.406 | D | 0.892 | 1.218 |
| | 15 | 0.502 | P | 0.808 | 1.136 |
| | 16 | 0.583 | D | 0.856 | 1.142 |
| | 17 | 0.453 | D | 0.874 | 1.971 |
| | 18 | 0.371 | xl | 0.87 | 1.132 |
| | 19 | 0.292 | xl | 0.903 | 1.156 |
| | 20 | 0.515 | xl | 0.884 | 1.230 |
| | 21 | 0.481 | D | 0.893 | 1.282 |
| | 22 | 0.632 | xl | 0.908 | 1.249 |
| | 23 | 0.418 | P | 0.86 | 1.332 |
| | 24 | 0.493 | xl | 0.918 | 1.333 |
| | 25 | 0.370 | D | 0.886 | 1.285 |
| | 26 | 0.310 | D | 0.889 | 1.243 |
| | 27 | 0.345 | D | 0.901 | 1.111 |
| | 28 | 0.380 | D | 0.905 | 1.152 |
| | 29 | 0.679 | xl | 0.904 | 1.214 |
| | 30 | 0.418 | xl | 0.899 | 1.060 |
| **2 phi** | 1 | 0.131 | P | 0.833 | 1.645 |
| | 2 | 0.078 | P | 0.845 | 1.525 |
| | 3 | 0.237 | P | 0.635 | 1.460 |
| | 4 | 0.208 | P | 0.666 | 1.909 |
| | 5 | 0.362 | P | 0.665 | 2.155 |
| | 6 | 0.213 | D | 0.858 | 1.127 |
| | 7 | 0.166 | P | 0.734 | 1.885 |
| | 8 | 0.300 | D | 0.715 | 2.270 |
| | 9 | 0.197 | D | 0.794 | 2.118 |
| | 10 | 0.183 | D | 0.693 | 1.504 |
| | 11 | 0.194 | P | 0.718 | 1.662 |

| | | | | | |
|---|---|---|---|---|---|
| | 12 | 0.160 | P | 0.696 | 2.084 |
| | 13 | 0.196 | P | 0.692 | 1.195 |
| | 14 | 0.120 | P | 0.742 | 1.650 |
| | 15 | 0.096 | P | 0.814 | 1.314 |
| | 16 | 0.140 | P | 0.71 | 1.272 |
| | 17 | 0.159 | P | 0.621 | 1.641 |
| | 18 | 0.314 | P | 0.679 | 1.913 |
| | 19 | 0.179 | P | 0.755 | 1.212 |
| | 20 | 0.195 | P | 0.687 | 2.557 |
| | 21 | 0.100 | P | 0.844 | 1.421 |
| | 22 | 0.117 | P | 0.858 | 1.824 |
| | 23 | 0.080 | P | 0.883 | 1.158 |
| | 24 | 0.211 | P | 0.771 | 2.417 |
| | 25 | 0.066 | D | 0.807 | 1.401 |
| | 26 | 0.140 | P | 0.723 | 1.527 |
| | 27 | 0.172 | P | 0.795 | 1.541 |
| | 28 | 0.201 | P | 0.803 | 2.298 |
| | 29 | 0.287 | D | 0.702 | 1.711 |
| | 30 | 0.114 | D | 0.701 | 2.609 |
| **3 phi** | 1 | 0.067 | P | 0.794 | 1.878 |
| | 2 | 0.035 | P | 0.732 | 2.954 |
| | 3 | 0.038 | P | 0.719 | 1.832 |
| | 4 | 0.027 | D | 0.797 | 1.092 |
| | 5 | 0.026 | P | 0.697 | 1.393 |
| | 6 | 0.034 | P | 0.649 | 1.104 |
| | 7 | 0.041 | D | 0.832 | 1.400 |
| | 8 | 0.030 | P | 0.675 | 1.423 |
| | 9 | 0.036 | P | | 1.341 |
| | 10 | 0.052 | P | 0.652 | 1.410 |
| | 11 | 0.038 | P | 0.761 | 1.435 |
| | 12 | 0.039 | P | 0.775 | 1.623 |
| | 13 | 0.023 | P | 0.545 | 1.473 |
| | 14 | 0.079 | P | 0.572 | 1.874 |
| | 15 | 0.024 | P | 0.698 | 1.292 |
| | 16 | 0.048 | P | 0.535 | 2.642 |
| | 17 | 0.060 | D | 0.719 | 2.332 |
| | 18 | 0.044 | D | 0.759 | 2.033 |
| | 19 | 0.028 | P | 0.558 | 1.225 |
| | 20 | | D | | |
| | 21 | 0.044 | D | 0.675 | 2.191 |

| | | | | | |
|---|---|---|---|---|---|
| | 22 | | P | | |
| | 23 | 0.042 | P | 0.72 | 4.079 |
| | 24 | | P | | |
| | 25 | 0.029 | P | 0.685 | 1.865 |
| | 26 | 0.036 | P | 0.598 | 1.626 |
| | 27 | | D | | |
| | 28 | 0.034 | P | 0.591 | 2.150 |
| | 29 | 0.033 | P | 0.774 | 1.721 |
| | 30 | | P | | |
| **4 phi** | 1 | 0.007 | P | 0.797 | 1.386 |
| | 2 | | P | | |
| | 3 | 0.004 | P | 0.757 | 1.597 |
| | 4 | 0.007 | P | 0.743 | 2.039 |
| | 5 | 0.009 | xl | 0.898 | 1.292 |
| | 6 | 0.010 | D | 0.818 | 1.542 |
| | 7 | 0.006 | P | 0.818 | 1.172 |
| | 8 | 0.007 | P | 0.646 | 1.443 |
| | 9 | 0.006 | D | 0.649 | 2.040 |
| | 10 | 0.007 | P | 0.72 | 1.361 |
| | 11 | 0.005 | P | 0.719 | 1.679 |
| | 12 | 0.009 | D | 0.834 | 1.332 |
| | 13 | 0.005 | P | 0.747 | 1.053 |
| | 14 | 0.005 | P | 0.731 | 1.706 |
| | 15 | 0.005 | P | 0.764 | 1.977 |
| | 16 | 0.005 | P | 0.724 | 1.732 |
| | 17 | | P | | |
| | 18 | | D | | |
| | 19 | 0.004 | P | 0.669 | 1.110 |
| | 20 | 0.005 | P | 0.689 | 1.520 |
| | 21 | 0.007 | P | 0.672 | 1.417 |
| | 22 | 0.006 | P | 0.654 | 1.540 |
| | 23 | 0.009 | D | 0.666 | 1.245 |
| | 24 | 0.007 | P | 0.722 | 1.923 |
| | 25 | 0.004 | P | 0.589 | 1.060 |
| | 26 | 0.008 | P | 0.764 | 1.275 |
| | 27 | 0.007 | P | 0.777 | 1.074 |
| | 28 | | P | | |
| | 29 | 0.007 | P | 0.679 | 1.220 |
| | 30 | 0.015 | P | 0.69 | 1.363 |

# References


Bandfield, J. L., Hamilton, V. E., and Christensen, P. R. (2000). A global view of martian surface compositions from MGS-TES. *Science*, 287(5458), 1626–1630.

Bradley, B. A., Sakimoto S. E. H., Frey, H., and Zimbleman, J. R. (2002). Medusae Fossae Formation: New perspectives from Mars Global Surveyor. *Journal of Geophysical Research: Planets*, 107(E8), doi: 10.1029/2001JE001537.

Edgett, K. S. (1997). Aeolian dunes as evidence for explosive volcanism in the Tharsis Region of Mars. *Icarus*, 130(1), 96–114.

Fagents, S. A., Baloga, S. M., Fitch, E. P., and Langdalen, Z. L. (2017). Dispersal of ash in the Martian atmosphere. *Geological Society of America Cordilleran Section Meeting*, Honolulu, HI, May 23–25, 2017.

Fitch, E. P., Fagents, S.A., Thordarson, T., and Hamilton, C.W. (2017). Fragmentation mechanisms associated with explosive lava–water interactions in a lacustrine environment. *Bulletin of Volcanology*, 79(12), doi: doi:10.1007/s00445-016-1087-3.

Glaze, L. S., and Baloga, S. M. (2002). Volcanic plume rise heights on Mars: Limits of validity for convective models. *Journal of Geophysical Research,* 107(E10), doi:10.1029/2001JE001830.

Greeley, R., Bridges, N. T., Crown, D. A., Crumpler, L. S., Fagents, S. A., Mouginis-Mark, P. J., and Zimbelman, J. R. (2000). Volcanism on the Red Planet: Mars, *in Environmental Effects on Volcanic Eruptions: From Deep Oceans to Deep Space* J. R. Zimbelman and T. K. P. Gregg (eds.), Kluwer/Plenum, 75–112.

Hartmann, W. K., and Neukum, G. (2001). Cratering chronology and the evolution of Mars. *Space Science Reviews,* 96, 165–194.

Hynek, B. M., Phillips, R. J., and Arvidson, R. E. (2003). Explosive volcanism in the Tharsis region: Global evidence in the martian geologic record. *Journal of Geophysical Research: Planets*, 108(E9), doi:10.1029/2003JE002062.

Janebo, M. H., Thordarson, Th., Houghton, B. F., Bonadonna, C., Larsen, G., and Carey, R. J. (2016). Dispersal of key subplinian–Plinian tephras from Hekla volcano, Iceland. *Bulletin of Volcanology*, *78*(10), doi:10.1007/s00445-016-1059-7.

Kerber, L., Head, J. W., Madeleine, J. B., Forget, F., and Wilson, L. (2012). The dispersal of pyroclasts from ancient explosive volcanoes on Mars: Implications for the friable layered deposits. *Icarus*, 219(1), 358–381.

Kerber, L., Francois, F., Madeleine, J. B., Wordsworth, R., Head, J. W., and Wilson, L., (2013). The effect of atmospheric pressure on the dispersal of pyroclasts from martian volcanoes. *Icarus*, 223, 149–156.

Ogliore, R. C., and Jilly, C. E. (2013). Gigapixel optical microscopy for meteorite characterization. *Planetary Science*, 2(3), doi: doi:10.1186/2191-2521-2-3.

Malin, M. C., and Edgett, K. S. (2000). Evidence for recent groundwater seepage and surface runoff on Mars. *Science*, 288(5475), 2330–2335.

Scott, D. H., and Tanaka, K. L. (1982). Ignimbrites of Amazonis Planitia region of Mars. *Journal of Geophysical Research: Solid Earth*, 87(B2), 1179–1190.

Werner, S. C. (2009). The global martian volcanic evolutionary history. *Icarus*, 201(1), 44–68.

[redacted]

White, J. D. L., and Houghton, B. F. (2006). Primary volcaniclastic rocks. *Geology*, 34(8), 677–680.